Automatic Target Recognition Using Passive Radar and a Coordinated Flight Model

A Thesis
Presented to
The Academic Faculty

by

Lisa M. Ehrman

In Partial Fulfillment
of the Requirements for the Degree
Master of Science in Electrical and Computer Engineering

School of Electrical and Computer Engineering
Georgia Institute of Technology
May 2004

Automatic Target Recognition Using Passive Radar and a Coordinated Flight Model

Approved by:

Professor Aaron Lanterman, Advisor

Professor Paul Steffes

Professor Doug Williams

Date Approved

To my wonderful husband, Brad.

ACKNOWLEDGEMENTS

This work was funded by the NATO Consultation, Command, and Control Agency (NC3A), as well as by start-up funds from the School of Electrical and Computer Engineering at the Georgia Institute of Technology. I would like to thank Dr. Paul Howland and Dr. Rene van der Heiden at NC3A for their support. I would also like to thank my advisor, Professor Aaron Lanterman, for his encouragement and assistance over the past year. I am also indebted to Major Larkin Hastriter and Lt. Col. Adam MacDonald for their assistance in obtaining aircraft flight paths. Finally, I would like to thank Professor Lakshmi Sankar of the School of Aerospace Engineering at the Georgia Institute of Technology for his patience and guidance.

TABLE OF CONTENTS

LIST OF TABLES

LIST OF FIGURES

SUMMARY

Rather than emitting pulses, passive radar systems rely on illuminators of opportunity, such as TV and FM radio, to illuminate potential targets. These systems are particularly attractive since they allow receivers to operate without emitting energy, rendering them covert. Many existing passive radar systems estimate the locations and velocities of targets. This thesis focuses on adding an automatic target recognition (ATR) component to such systems.

The proposed approach to ATR compares the Radar Cross Section (RCS) of targets detected by a passive radar system to the simulated RCS of known targets. To make the comparison as accurate as possible, the received signal model accounts for aircraft position and orientation, propagation losses, and antenna gain patterns. The estimated aircraft positions become inputs to an algorithm that uses a coordinated flight model to compute probable aircraft orientation angles. The Fast Illinois Solver Code (FISC) simulates the RCS of several potential target classes as they execute the estimated maneuvers. The RCS is then scaled by the Advanced Refractive Effects Prediction System (AREPS) code to account for propagation losses that occur as functions of altitude and range. The Numerical Electromagnetic Code (NEC2) computes the antenna gain pattern, so that the RCS can be further scaled. A Rician likelihood model compares the RCS of the illuminated aircraft with those of the potential targets. This comparison results in target identification.

Results are presented for a variety of possible aircraft flight paths, and for both HH and VV polarizations. Algorithm performance is found to be highly dependent upon the achieved signal-to-noise ratio (SNR), and is also affected by the accuracy of the position estimates. The results are generally quite good when the signal power is greater than the noise power and the position is accurately known; however, some significant performance degradation is noted for one aircraft type when the HH polarization is used.

CHAPTER I

INTRODUCTION

1.1 History of the Problem

There are two parallel schools of thought prevalent in the literature regarding the recognition of fast-moving fixed-wing aircraft. The first approach proposes the creation of target images, such as two-dimensional inverse synthetic aperture radar (ISAR) images or a sequence of one-dimensional range profiles [10]. Target recognition is then conducted using these images. The alternate approach has been to bypass the creation of images and attempt recognition directly from the received data. Following the path suggested in [12], Herman takes this second approach to automatic target recognition (ATR), using data obtained from a passive radar system [8, 7].

Although ATR has been a subject of much research, Herman's application of passive radar was innovative. Unlike traditional radar systems, passive radar systems bypass the need for dedicated transmitters by exploiting "illuminators of opportunity" such as commercial television and FM radio signals. In doing so, they are able to reap a number of benefits. Most notably, the fact that passive radar systems do not emit energy renders them covert; this is a great strategic advantage if the systems are employed by the military. Passive radar systems may also be much less expensive than traditional ones, where most of the cost is associated with the transmitter.

Additionally, many illuminators of opportunity employ low frequencies. Although passive radar systems do not inherently require these low frequencies, the allocation of bandwidth for commercial TV and FM radio implies that passive radar systems operate at lower frequencies than traditional microwave radar. As a fortunate though unintended consequence, the low-frequency signals exploited by passive radar are well-suited for ATR [14, 13, 2]. In addition to being less susceptible to inclement weather, the longer wavelengths result in target radar cross sections that vary "slowly" with small changes in the

target state vector. Herman noted that the variation in radar cross section (RCS), as characterized by the number of nulls encountered as a target's aspect changes, is proportional to the electrical length of the target [8, 7]. At FM-band frequencies (100 MHz), a fighter-sized aircraft is approximately five wavelengths long. In contrast, at the X-band frequencies used by many traditional radars (10 GHz), the same aircraft would be 500 wavelengths long, making the ATR system very sensitive to small changes in target orientation.

Despite its numerous benefits, passive radar was once deemed impractical. In the mid-1980s, Griffiths and Long [6] attempted to extract range information from backscattered television signals. Plagued by the low signal-to-noise ratio resulting from the available equipment and the range ambiguity inherent in the sync pulses of an analog TV signal, their results did not seem encouraging. A decade later, Howland [9] successfully tracked targets by abandoning any attempt to directly measure range in favor of the velocity information contained in the Doppler-shifted TV carrier and the angle-of-arrival information derived from a simple two-antenna array. Exotic track initialization algorithms, combined with an extended Kalman filter, fuse the Doppler and angle-of-arrival information into Cartesian coordinate tracks.

Today, several passive radar systems are in operation. The most widely tested manifestation of this kind of technology is probably the Silent Sentry series developed by Lockheed Martin Mission Systems of Gaithersburg, MD, which can exploit both analog television and FM radio signals. Another well-known system is the Manastash Ridge Radar[1] developed by John Sahr at the University of Washington [18, 19], which uses FM radio-based passive radar for atmospheric studies.

1.2 A New Approach to ATR

The primary goal of this research is to add ATR capabilities to existing passive radar systems, using RCS as the key information for classification. Since RCS is highly aspect-dependent, accurate estimation of target orientation is crucial. Herman [8, 7] met this challenge with a computationally intensive particle filter [3], which jointly estimated target

[1] www-rcs.ee.washington.edu/~radar/Projects/Manastash

position, orientation, and target type. This thesis seeks a less computationally intensive approach. The positions and velocities estimated by the existing passive radar system are considered to be "true." They are then exploited by a coordinated flight model [5] to estimate aircraft orientation.

A database of Fast Illinois Solver Code (FISC) results is created for each aircraft in the target class. This database is accessed using the aircraft orientations estimated by the coordinated flight model. This results in a set of power profiles simulating those that would arrive at the receiver if the aircraft in the target class were executing the maneuver. These profiles are then scaled for propagation losses and antenna gain of the receiver using the Advanced Refractive Effects Prediction System (AREPS) and Numerical Electromagnetic Code (NEC2), respectively. Finally, the profiles corresponding to members of the target class are compared to the profile of the actual target, resulting in target identification.

The work presented here is simulation-based. Target profiles arriving at the receiver are simulated by adding white Gaussian noise to the profile. One hundred such noisy profiles are created for each member of the target class for each scenario to create a statistically significant set of simulations. It is worth noting that the aircraft comprising the target classes are chosen based upon the availability of acceptable CAD models, rather than likelihood of occurrence near a real system. A secondary goal of this research is to model a system currently being developed by NATO/NC3A with the intent of an eventual comparison with real data. At that point, more realistic target classes will be implemented.

CHAPTER II

COORDINATED FLIGHT MODEL

Given that target RCS is the sole factor used to classify the aircraft, its accurate representation is paramount. This task is hardly trivial, as RCS is heavily dependent upon the incident and observed angles, which in turn are dependent upon the yaw, heading, pitch, and roll of the aircraft. This chapter presents a coordinated flight model to estimate these angles, given a set of time-correlated aircraft positions.

2.1 Coordinate Conventions

The conventions used for yaw, pitch, and roll are depicted in Figure 1a. The convention used in the computation of aircraft heading is shown in Figure 1b; this complies with typical navigational conventions.

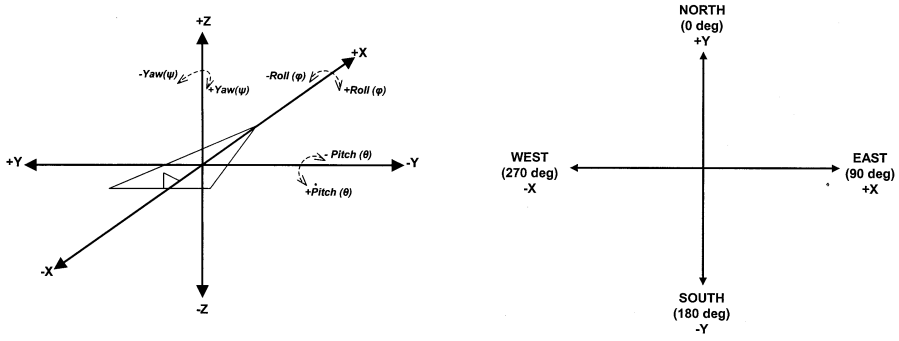

Figure 1: Coordinate conventions: a) yaw, pitch, and roll (left) b) heading (right).

2.2 Aircraft Yaw

As shown in Figure 1a, the yaw of an aircraft describes the angular difference in the x-y plane between the aircraft's velocity vector and the direction of the aircraft nose. Conditions such as high wind and severe weather sometimes induce yaw in aircraft flight; however, under

normal circumstances, the yaw for fast-moving, fixed-wing aircraft is approximately zero. For this reason, this thesis assumes that yaw is always zero.

2.3 Aircraft Heading

Aircraft heading describes the association of cardinal directions with aircraft motion in the x-y plane. The convention adopted by this thesis is shown in Figure 1b, and is consistent with standard navigational practices. Since heading is a function of aircraft motion in the x-y plane, it can be written as a function of the x and y components of aircraft velocity. The equation for aircraft heading is given by,

$$\xi = \begin{cases} 90 - \arctan(\frac{v_Y}{v_X}), x > 0 \\ 270 - \arctan(\frac{v_Y}{v_X}), x < 0 \end{cases} . \tag{1}$$

Since the equation provides a linear approximation, it is most accurate when the time between aircraft position samples is small.

2.4 Aircraft Pitch

The pitch of an aircraft describes the angle between the total velocity vector and the velocity vector in the x-y plane, and can be thought of as the angle at which the aircraft is changing altitude. Let (dx, dy, dz) denote the difference in aircraft position over a period of time, dt. The pitch is then given by,

$$\theta = \arctan\left(\frac{dz}{\sqrt{dx^2 + dy^2}}\right). \tag{2}$$

Although this is a linear approximation, it should provide sufficient accuracy as long as the sampling rate of aircraft position is fairly high.

2.5 Aircraft Roll

Figure 1a depicts aircraft roll as the rotation of the aircraft about the vector that comes out of the aircraft nose in the direction of aircraft motion. This rotation can be performed

by many high-performance aircraft without any deviation in the flight path or velocity, rendering it impossible to compute the roll angle as a function of flight path with a high degree of certainty. One option is to compute probable orientation angles, based upon a flight path. With that in mind, non-zero roll angles are considered to be the likeliest orientation only when the aircraft is executing a turn. In all other circumstances, the roll is assumed to be zero.

2.5.1 Constant Altitude: A Special Case

The easiest approach to computing aircraft roll is to begin with a case in which the aircraft is executing a constant-altitude banked turn of radius R. A free body diagram of an aircraft executing such a turn is shown in Figure 2.

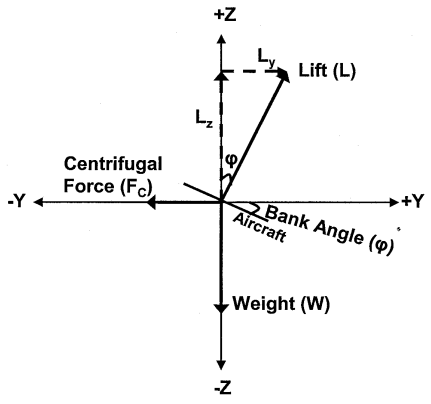

Figure 2: Free body diagram of an aircraft executing a constant-altitude banked turn.

Since this is assumed to be a coordinated turn, no slipping can occur in the aircraft's lateral axis. Equivalently, the sum of the forces in the y-direction is equal to zero. From Figure 2 it is clear that the forces acting in the y-direction are the centrifugal force, F_C, and the y-component of the aircraft lift, L_Y. Thus, it is possible to write

$$L_Y = F_C. \tag{3}$$

The centrifugal force is derived from Newton's Second Law, in which $\frac{W}{g}$ is substituted for mass and $\frac{|v|^2}{R}$ is substituted for acceleration. Here, W is the weight and g is the standard gravity at Earth's surface. The y-component of lift is related to the total lift through a

simple trigonometric relation. Substitution of these expressions into (3) results in

$$L\sin(\phi) = \frac{W|v|^2}{Rg}. \tag{4}$$

Solving (4) for the roll angle yields

$$\phi = \arcsin\left(\frac{W|v|^2}{LRg}\right). \tag{5}$$

Since the aircraft is maintaining a constant altitude, the sum of the forces in the z-direction is also equal to zero. Figure 2 demonstrates that the forces acting in the z-direction are the weight, W, and the z-component of the lift, L_Z. Thus,

$$L_Z = W, \tag{6}$$

describes the equilibrium of forces in the z-direction. L_Z can be written as a function of total lift, L, and roll angle. This relation is substituted into (6), resulting in

$$L\cos(\phi) = W, \tag{7}$$

which can be solved for the roll angle, giving

$$\phi = \arccos\left(\frac{W}{L}\right). \tag{8}$$

Both weight and lift vary with aircraft type, which is unknown [11]. For this reason, it would be advantageous to derive an equation for the roll angle that is independent of weight and lift. Fortunately, this can be accomplished by combining (5) and (8) to give

$$\phi = \arctan\left(\frac{|v|^2}{Rg}\right). \tag{9}$$

The aircraft velocity can be easily derived from the aircraft flight path, and the standard gravity at Earth's surface is a known constant. Thus, the only remaining unknown in (9) is the radius of the turn.

Computing the radius of the turn would be relatively simple if aircraft always flew in perfect circles and began the turns instantaneously. However, this is not the case. Even if an aircraft were able to instantaneously snap into banked turns, the instantaneous G-loading

induced by such maneuvers could be harmful for pilots. For this reason, it is common practice for aircraft to gradually transition into banked turns.

This gradual transition can be thought of as moving from a turn with a radius of curvature approaching infinity to a turn with a particular finite radius. Similarly, the transition out of a banked turn can be treated as moving from a turn with a finite radius to one with a radius approaching infinity. Thus, the transition made by an aircraft into or out of a banked turn is essentially just a curve with a uniformly changing degree of curvature. This type of curve is known as a spiral curve.

The radius of curvature at any point along a spiral curve can be found using the method of osculating circles. In this method, a "circular arc drawn tangent to the spiral at point P has a radius r equal to the radius of curvature of the spiral at the point of tangency" [17]. The circular arc is known as an osculating circle, whose radius of curvature is given by

$$R_{XY}(t) = \frac{[\dot{x}(t)^2 + \dot{y}(t)^2]^{3/2}}{\dot{x}(t)\ddot{y}(t) - \ddot{x}(t)\dot{y}(t)}, \tag{10}$$

where $x(t)$ and $y(t)$ are the x and y positions as functions of time. Using this method, the radius of curvature can be found for every position in the flight path. The resulting radius function can be substituted into (9) to compute roll as a function of time.

The sign of the roll angle must also be considered. Because the expression for roll given by (9) is a function of the magnitude of the velocity, the radius of acceleration, and the standard gravity at Earth's surface, it always results in a positive roll angle. From Figure 1a, it is clear that positive roll angles are associated with rolls in which the aircraft's right wing is down. If the aircraft is flying in a clockwise manner, then the roll angle should be positive, given the current convention. Conversely, counter-clockwise flight should result in negative roll angles.

A simple way to implement this convention is to test for counter-clockwise flight, and invert the sign of the roll angle when it is detected. A logical test for counter-clockwise flight in a certain incremental period of time, dt, is given by

$$[(dx < 0) \text{ and } (\text{CU})] \text{ or } [(\text{dx} > 0) \text{ and } (\text{CD})], \tag{11}$$

where CU denotes a flight path that is concave-up during dt, CD denotes a flight path that is concave-down during dt, and dx is the incremental signed distance traversed by the aircraft in the x-direction during dt. Applying this test to the values computed with (9) results in the computation of aircraft roll in accordance with the conventions selected in Figure 1.

2.5.2 General Case

Until now, the derivation of aircraft roll has assumed that the aircraft maintains a constant altitude while turning. This methodology must be expanded to account for the possibility that the aircraft changes altitude as it maneuvers. The key issue which must be addressed to account for varying altitudes is that the sum of forces in the z-direction is no longer equal to 0. Thus, Equations 6 through 9 correspond to a special case that is not valid if the aircraft changes altitude while turning.

One solution to this dilemma is to select a coordinate system in which the aircraft is not changing altitude. This is accomplished by first rotating the x-y plane such that all of the motion in the new x'-y' plane occurs in the +x'-direction. If this is followed by a rotation of the x'-z plane, then all of the aircraft motion in the newly-created x"-y'-z' space will be parallel to the x"-axis. Note that this process must be repeated at every time increment to account for varying aircraft pitch. Consider the aircraft motion over the incremental time, dt, shown in Figure 3a. The aircraft motion depicted in Figure 3a is non-zero in both the x and y directions. The x-y plane is then rotated so that all aircraft motion in the plane occurs in the +x'-direction. The result of this rotation is shown in Figure 3b. For the aircraft to be in equilibrium in the new coordinate space, the x-z plane needs to be rotated by the pitch angle. The resulting geometry is shown in Figure 3c.

Once the new coordinate systems have been established, the problem is nearly identical to the constant-altitude problem. The resulting free body diagram is shown in Figure 4.

Equations 3 through 8 are used, but require minor modifications in order to apply to the new coordinate system. Due to the rotations, the sum of forces in the y'-direction is

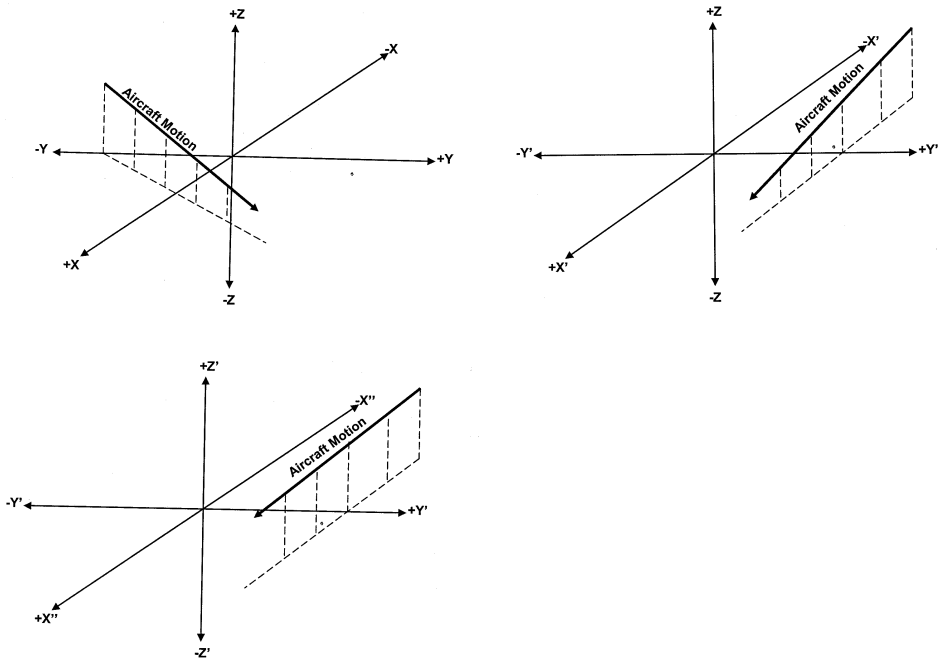

Figure 3: Aircraft motion : a) x-y-z space (top left) b) x'-y'-z space (top right) c) x"-y'-z' space (bottom left).

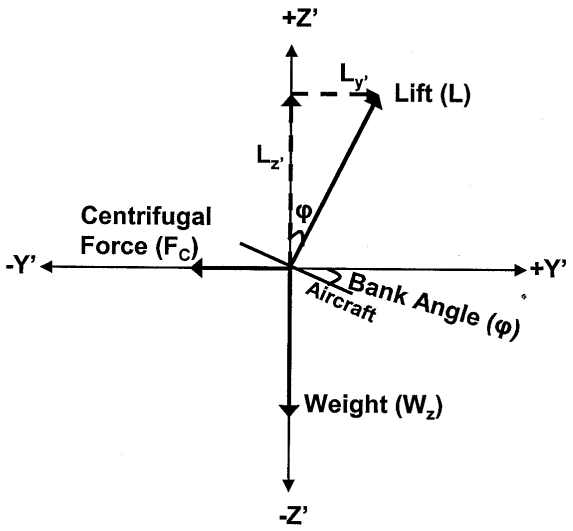

Figure 4: Free body diagram of an aircraft executing a varying-altitude banked turn.

equal to zero, meaning that

$$L_{Y'} = F_C. \tag{12}$$

Care must be taken when computing the centrifugal force in the new coordinate system. Recall that the centrifugal force is derived from Newton's Second Law. The mass term in Newton's Second Law is replaced by

$$m = \frac{W_z}{g}. \tag{13}$$

Even though the z-axis has been rotated to create the z'-axis, the weight still acts in the direction of the -z-axis. The acceleration term in Newton's Second Law, or radial acceleration in this case, is now dependent upon the radius of curvature that exists in the x"-y' plane rather than the x-y plane. Keeping this in mind, (12) is rewritten as

$$L\sin(\phi) = \frac{W_z|v|^2}{R_{x''y'}g}, \tag{14}$$

which is solved for the roll such that

$$\phi = \arcsin\left(\frac{W_z|v|^2}{LR_{x''y'}g}\right). \tag{15}$$

Equations 6 through 8 can be applied as well, but minor changes are needed. Since the sum of forces in the z'-direction is equal to zero, it is possible to write

$$L_{z'} = W_{z'}. \tag{16}$$

Note that only the z' components of lift and weight are used in (16). Using trigonometric relations, (16) is expanded to

$$L\cos(\phi) = W_z\cos(\theta), \tag{17}$$

where θ is the pitch angle. Solving for the roll angle results in

$$\phi = \arccos\left(\frac{W_z\cos(\theta)}{L}\right). \tag{18}$$

Now (15) and (18) are combined, resulting in

$$\phi = \arctan\left(\frac{|v|^2\cos(\theta)}{R_{x''y'}g}\right). \tag{19}$$

The radius of curvature in the x"-y' plane is given by

$$R_{x''y'}(t) = \frac{[\dot{x}''(t)^2 + \dot{y}'(t)^2]^{3/2}}{\dot{x}''(t)\ddot{y}'(t) - \ddot{x}''(t)\dot{y}'(t)}. \quad (20)$$

Equation 19 provides a general equation for the roll angle that can be applied to the entire flight path. For example, when the aircraft maintains a constant altitude, θ is zero, and x" is identical to x. Under these circumstances, the radius of curvature in the x-y plane equals that in the x"-y' plane. Thus, when the aircraft maintains a constant altitude, (19) reduces to (9). Equation 19 also applies when the aircraft flies in a straight line. In such a case, the radius of curvature given by (20) approaches infinity, driving the roll angle to zero.

2.6 Testing the Coordinated Flight Model

A strenuous test of the algorithm was conducted using data collected during the F-15C Joint Helmet Cuing System mission JH-16, conducted by the 445th Flight Test Squadron at Edwards Air Force Base in May 2000. Position, pitch, and roll were recorded on board the aircraft. The aircraft heading was computed after the flight based upon the aircraft position data. The time-correlated positions were extracted from the data set to create a flight path, which serves as the input for the algorithm. The results of the algorithm were then compared to the real measured orientation angles. A 3-D view of the Edwards trajectory appears in the left panel of Figure 5, while position in the x-y plane is shown on the right.

Equation 1 was used to compute the aircraft heading in the navigational coordinate system. The real and computed aircraft headings are shown in the top graph of Figure 6. The bottom graph depicts the angular difference between the real and computed heading.

The computed heading matches the true heading quite well. It slightly underestimates the true heading, with a mean angular error of 0.2 degrees and a standard deviation of 0.1 degrees. This is to be expected, since the true heading was computed after the fact based upon the same position data used by the algorithm.

Next, the aircraft pitch was computed using Equation 2. The top plot in Figure 7 shows the real and computed pitch, while the bottom plot shows the angular error between the

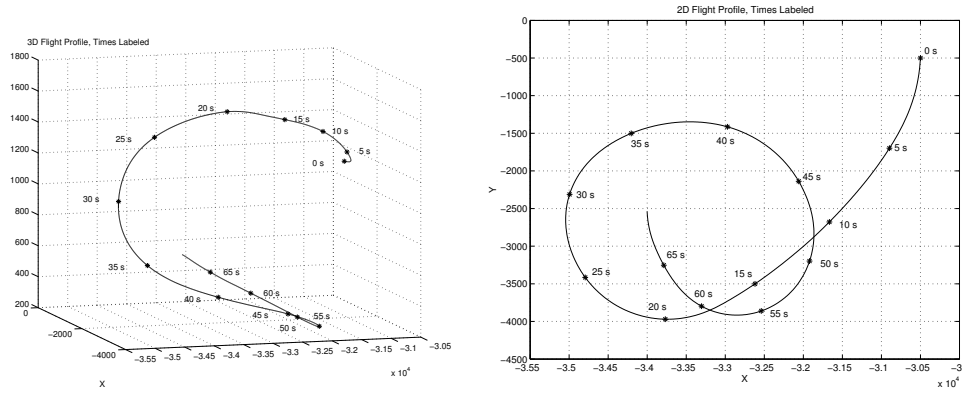

Figure 5: F-15 maneuver: a) 3-D view (left), b) top view (right).

two. The computed pitch shows good correlation with the pitch recorded on-board the F-15C. The coordinated flight model underestimates the pitch with a mean error of 3.1 degrees and a standard deviation of 2.3 degrees. The error in this case is attributed to the underlying assumption that the aircraft nose is pointed in the direction of the aircraft motion. The data suggests that this is a good approximation, but does not result in exact replication of the aircraft pitch. This issue will be explored further in future work.

Aircraft roll is the final parameter that is estimated by the algorithm. A comparison between the computed and real aircraft roll is shown in the top plot of Figure 8, while the bottom plot depicts the error between the two. In this case, the model underestimates the aircraft roll with a mean error of 1.5 degrees, and a standard deviation of 10.7 degrees. Although the mean error is not terribly large, the standard deviation reveals the difficulty of estimating aircraft roll from a flight path.

The difficulty in computing aircraft roll from a flight path is inherent to the problem. Modern aircraft are capable of executing roll maneuvers that do not manifest themselves in their flight paths. This renders precise determination of aircraft roll from a flight path an impossibility. The link between aircraft roll and position is simply less direct than is the case for heading and pitch. This, in turn, necessitates the need for the coordinated turn model. This model dictates that the aircraft does not slip at all in its lateral axis while executing the turn. While pilots often endeavor to fly perfectly coordinated turns, there are times when they do not; hence, the coordinated turn model may not always match reality.

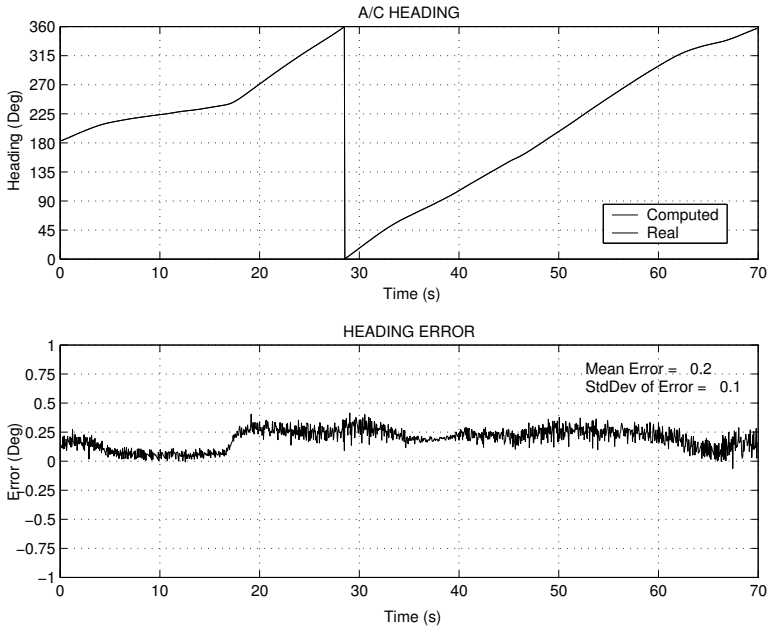

Figure 6: Comparison of real and computed aircraft heading.

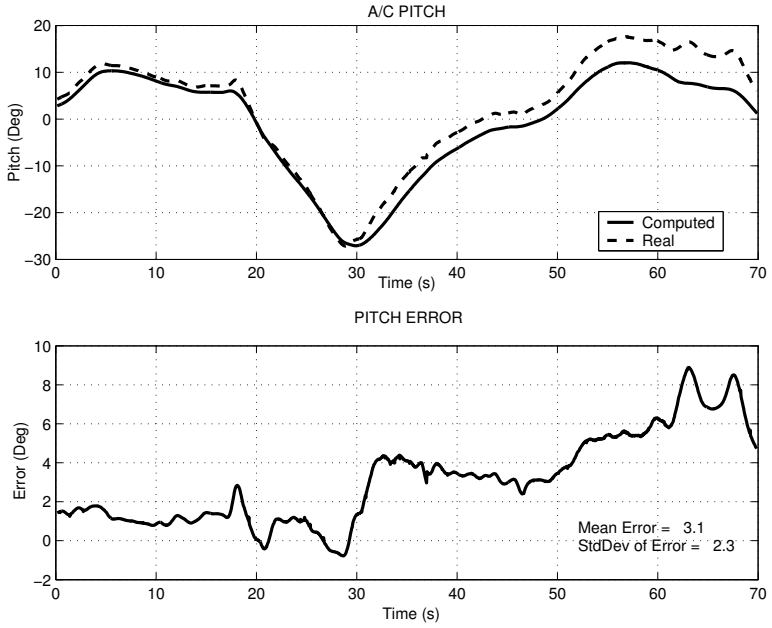

Figure 7: Comparison of real and computed aircraft pitch.

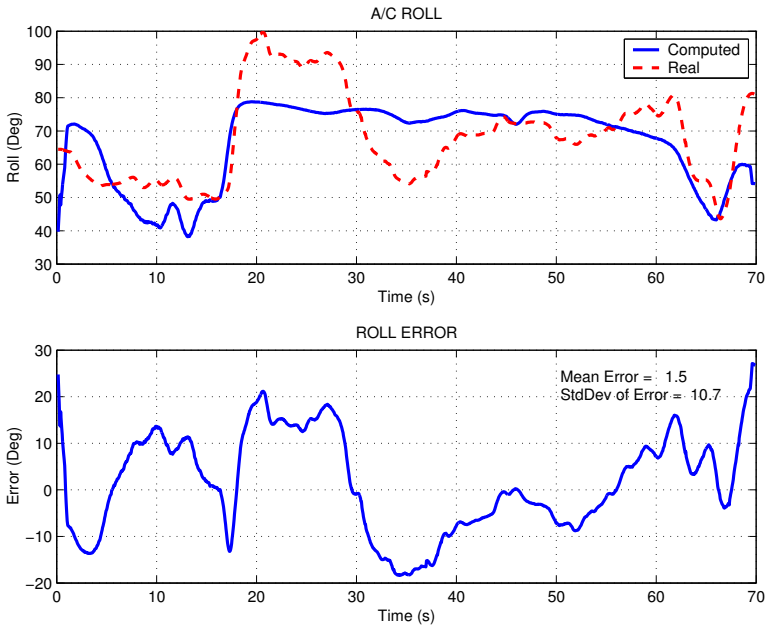

Figure 8: Comparison of real and computed aircraft roll.

CHAPTER III

TARGET CLASSIFICATION VIA MODELING

Once the aircraft orientation angles have been estimated, they are appended to the existing trajectory. This creates a supplemented flight profile. Together with the system geometry, this supplemented flight profile provides all the information necessary to access the RCS database.

3.1 System Description

The system parameters used in this work are selected to model a passive radar demonstration currently being developed by NATO. Table 1 shows the relevant parameters for the transmitter and receiver modeled in this research. Note that the NATO system uses vertically polarized antennas. The transmitter is shown in Figure 9a, while the receiver is shown in Figure 9b. The simulations presented in this thesis are conducted for both vertically polarized and horizontally polarized scenarios, to provide further insight into the viability of the algorithm.

Table 1: Transmitter and receiver parameters.

Parameter	Transmitter	Receiver
Latitude (N)	52^o 01' 00"	52^o 06' 36"
Longitude (E)	05^o 03' 00"	04^o 19' 26"
Altitude (m ASL)	375	100
Frequency (MHz)	100	–
Peak Power (kW)	100	–
Direction	Omni-Directional	320^o

3.2 Modeling Target Radar Cross Section

Modeling the power profile arriving at the receiving antenna is a multi-step process. The supplemented flight profile, containing aircraft position and orientation, is used to determine the incident and observed angles at every point during the encounter. The incident and

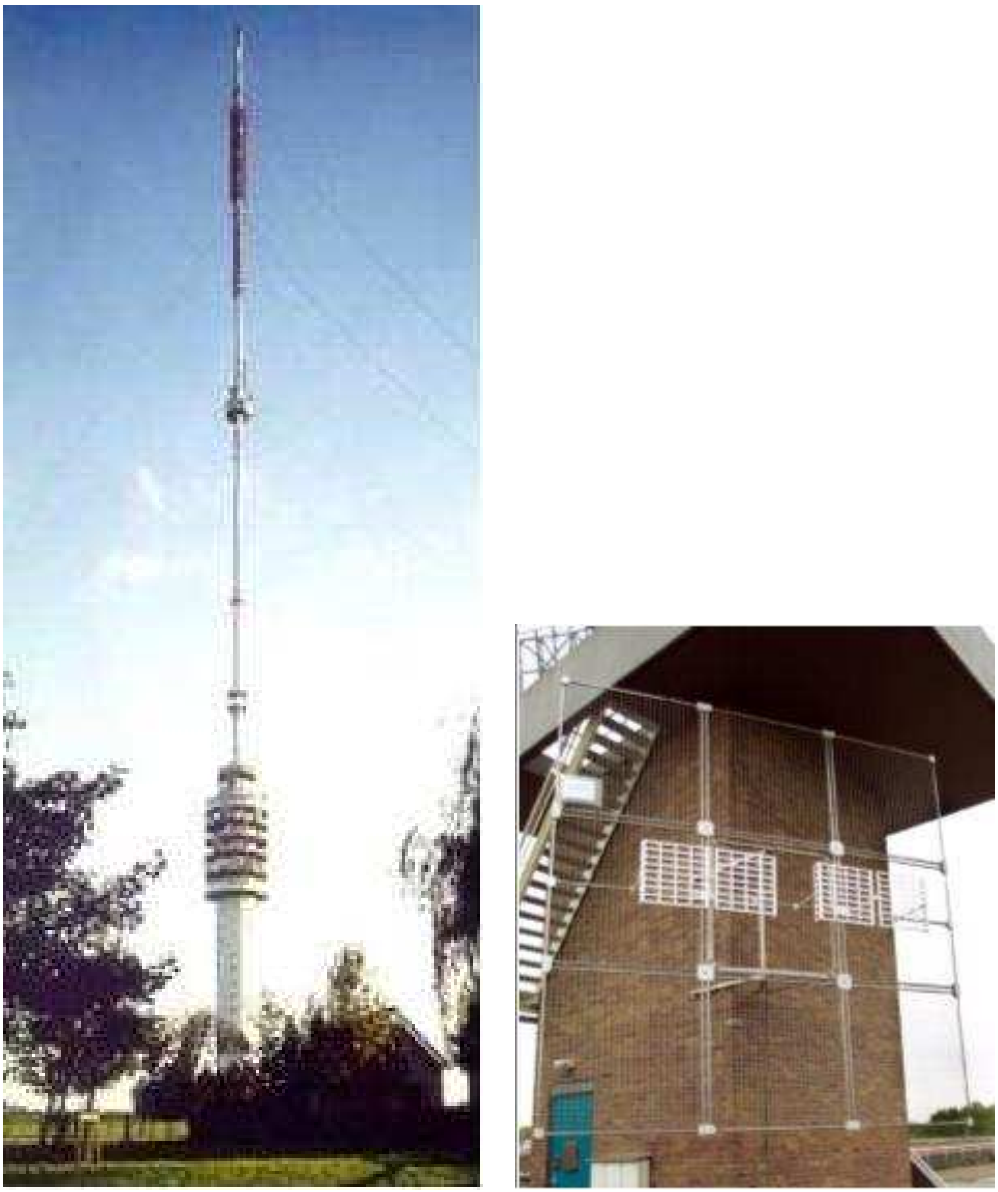

Figure 9: NATO NC3A antennas: a.) transmitter (left), b.) receiver (right).

observed angles are then used to access a database of FISC results which are available for each aircraft model in the target class. A set of power profiles are created when data is extracted from the RCS database. Additional scaling is required to make these power profiles represent the signals arriving at the receiver due to the illuminated targets. Some significant factors that must be considered are propagation losses between the aircraft and antennas, and antenna gain. The propagation losses, which include effects due to multipath, are modeled using AREPS. As is likely to be the case for most passive radar applications, the transmitting antenna exploited by the NATO system is omni-directional. Thus, the only antenna gain pattern that must be modeled corresponds to the receiver; this modeling is accomplished with NEC2. To cut down on the length of time required to execute the simulation, databases are also created for AREPS and NEC2. The overall result of this process is a power profile that is scaled to account for propagation losses and antenna gain.

A sample AREPS profile is shown in Figure 10a. This represents the propagation losses that occur between the transmitter an aircraft in a particular encounter. Note the sharp dip around 42 seconds. This artifact is attributed to coarse resolution in the AREPS database. The sharp point around 42 seconds rounds out as more points are included in an AREPS run. Despite the occasional artifact, the current size of the AREPS database provides a good tradeoff between database size and accuracy.

The antenna gain pattern of the receiver, modeled with NEC, is shown in Figure 10b. For the sake of the plot, zero elevation corresponds to the direction in which the antenna is aimed. The 360^o azimuth coverage traces out circles at the various elevations. Thus, the values for all 360 azimuths are the same when the elevation is 0, as they all point to the same relative location.

The necessity of the FISC database, as well as its limitations, are worth mentioning. Ideally, the simulation process described here would run FISC for every new set of incident and observed angles. However, the lengthy run-time and massive memory requirements of FISC render this option unfeasible. A more attractive option is the creation of a database of FISC results, in which aircraft RCS is sampled sufficiently to meet the Nyquist sampling

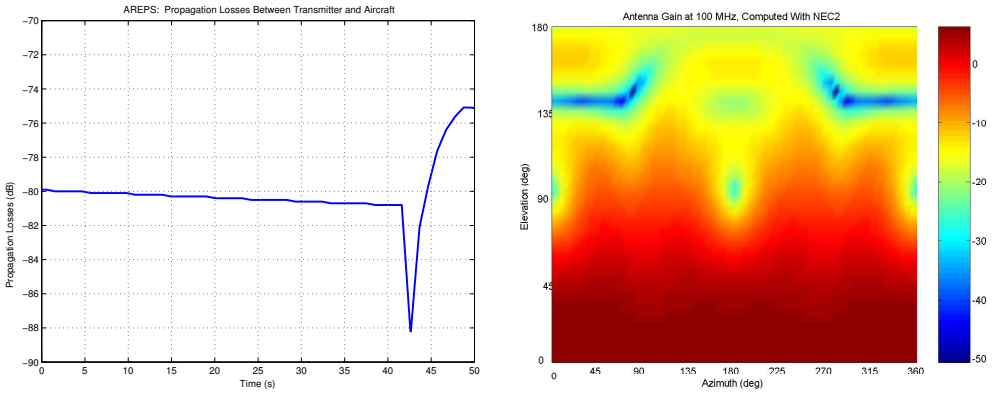

Figure 10: Scaling parameters: a.) sample AREPS profile (left), b.) antenna gain of receiver (right).

criterion. In particular, the angular sampling of the RCS should satisfy,

$$\Delta\theta \leq \frac{c}{(2f_0)(size)}, \tag{21}$$

where c is the speed of light, f_0 is the radar frequency, and $size$ is the longest dimension of the aircraft [16]. The minimum angular sampling required for each aircraft when the frequency is 100 MHz is shown in Table 2.

Table 2: Minimum angular sampling required for each aircraft in target class.

Aircraft	Longest Dimension (m)	Minimum Spacing (deg)
F-15	19.3	4.5
Falcon-20	17.1	5.0
Falcon-100	13.7	6.2
T-38	14.0	6.2

Thus, using an angular spacing of 4^o, a database of FISC runs can be created that is sufficiently full to represent the RCS of each aircraft type in the study, without aliasing. This database can be quickly accessed and allows for the creation of a power profile for virtually any desired flight path.

Although the profiles simulated by FISC are sampled as sparsely as possible while avoiding aliasing, the amount of time required to create a sufficiently large database remains daunting. At this point, the database has been completed for all combinations of observed

azimuths and elevations, and incident azimuths. However, the incident elevations available in the database[1] are currently limited to $\pm 20^o$. More sophisticated techniques will eventually be implemented to circumvent this limitation.

3.3 Modeling the Power Arriving at the Receiver

Recall that one goal of this research is to model a system currently being developed by NATO. Eventually, real power profiles may be available from the NATO receiver. Until then, it is necessary to simulate these profiles.

Two small changes differentiate this process from that used to find the precomputed RCS of known targets in the target class. First, when simulating the RCS of detected targets, the simulation is run with the real aircraft orientations in place of the estimated ones. These power profiles are then corrupted with additive white Gaussian noise, which acts independently on the real and imaginary parts of the signal. Along these lines, the simulated received profile is expressed as,

$$P_{SIM} = (\sqrt{P_R} + w_R)^2 + w_I^2, \tag{22}$$

where P_R is the real component of the power profile prior to being corrupted by noise, and w is zero-mean additive white Gaussian noise, which has real and imaginary components, w_R and w_I [7]. The noise power is computed in dBW using,

$$P_N = \frac{kT_0N_F}{CPI}, \tag{23}$$

where k is Boltzmann's constant, T_0 is temperature in Kelvin, N_F is the unitless noise figure, and CPI is the coherent processing interval of the system [1]. To match the NATO system, the CPI is set equal to 0.5 seconds, and T_0 is set equal to 290 K.

Selection of the noise figure, N_F, is more difficult. If the noise figure is only expected to account for thermal noise and out-of-band interference, then a conservative estimate of

[1]FISC requires a great deal of computational time to find the currents on the aircraft for a particular set of incident angles; however, once the model has been created for the set of incident angles, all of the possible pairs of observed angles can be computed relatively quickly. For this reason, the limited parameter in our database is the incident elevation.

the noise figure in a city environment might be 30 dB. In the absence of data regarding the noise power of the NATO system, it is reasonable to use this approximation.

To recap, the simulated received profiles are created by adding noise to the profiles generated using real orientation angles. In contrast, the library profiles used for target recognition result from using orientation angles estimated by the coordinated flight model.

3.4 Noise Power Due to Transmitter Interference

The noise figure accounts for thermal noise and out-of-band interference, but until now the issue of transmitter interference has not been addressed. Typically, this direct path interference manifests itself as a spike in the cross-ambiguity function. Since the transmitter's power and location are known, and since the direct path interference spike occurs along the axis with zero velocity, this spike can usually be identified and removed. The more treacherous effect of transmitter interference is that is can raise the "thumbtack" noise floor of the ambiguity function, potentially masking the target spike. To be thorough, this should also be considered when computing the noise figure.

If the ambiguity function is normalized such that the direct path spike has unit height, then the average pedestal height, or sideband power, is given by

$$P_{pedestal} = \frac{1}{B \times CPI}, \tag{24}$$

where B is the signal bandwidth, and CPI is the coherent processing interval [15]. To match the NATO system, values of 45 kHz and 0.5 seconds are used for B and CPI, respectively. If propagation losses and antenna gain are neglected, the pedestal power is 44 dBW below the direct-path spike. Since the NATO transmitter power is 50 dBW, the sideband power is 6 dBW. Propagation losses and antenna gain play a significant role, lowering the pedestal power by 95 dBW. The electronics in the receiver of the NATO system also mitigate the problem by suppressing the direct path signal by 70 dBW, which reduces the sideband power to -159 dBW. More sophisticated filters could be implemented to further reduce the noise figure, but using the specifications of the system being modeled, the effective noise figure falls between 40 and 45 dB. Thus, the effects due to transmitter interference are far more significant than those due to thermal noise and out-of-band interference.

To gain further insight into the impact of noise on the algorithm, the noise figure is swept from 30 dB to 100 dB in increments of 5 dB. The noise figures used in this thesis are shown in Table 3 along with the corresponding noise power. Note that noise figures above 45 dB are not anticipated in a real setting; they are merely included in this paper to demonstrate the breaking point of the classification algorithm.

Table 3: Noise figure and noise power.

Noise Figure (dB)	Noise Power (dBW)
30	-171
35	-166
40	-161
45	-156
50	-151
55	-146
60	-141
65	-136
70	-131
75	-126
80	-121
85	-116
90	-111
95	-106
100	-101

3.5 Target Identification

The simulation process is repeated for each member of the target class, resulting in a set of simulated radar cross sections corresponding to the detected targets. The automatic target recognizer compares these noisy received profiles to the library of precomputed power profiles. Equation 22 leads to a Rician likelihood model [7] whose probability density function is given by

$$p_x(x) = \frac{x}{\sigma_w^2} e^{\left(\frac{x^2+s^2}{2\sigma_w^2}\right)} I_0\left[\frac{xs}{\sigma_w^2}\right]. \tag{25}$$

To apply the Rician to the simulated and truth profiles, associate x with the magnitude of the RCS of the detected target, and s with the magnitude of the precomputed RCS of the target in the target class. The noise power, which equals the noise variance, is then

equated with σ_w^2. If each point in time is considered an independent sample from a process, then the data loglikelihood is

$$\ln(p_x(\bar{x})) = \sum_{i=1}^{n} \ln\left(I_0\left[\frac{x_i s_i}{\sigma_w^2}\right]\right) - \left(\frac{x_i^2 + s_i^2}{2\sigma_w^2}\right). \tag{26}$$

Loglikelihoods are computed for each member of the target class; the target is identified as the member of the target class with the largest loglikelihood [4].

CHAPTER IV

RESULTS OBTAINED USING VV POLARIZATION

Three scenarios of increasing complexity are presented to the algorithm. The locations of these three maneuvers relative to the system transmitter and receiver are shown in Figure 11.

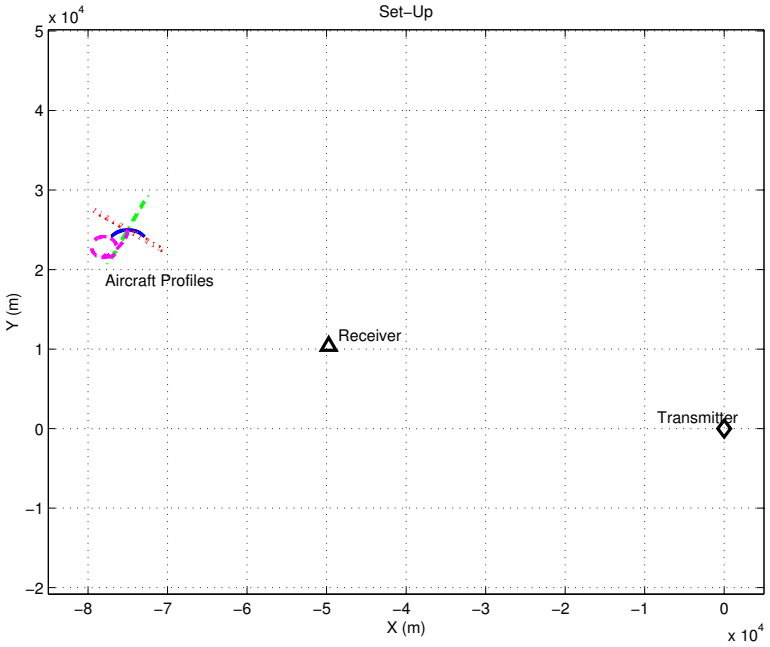

Figure 11: Maneuver locations relative to system transmitter and receiver.

The first scenario consists of a simple straight-and-level flight path. This does little to test the coordinated flight model, but gives a good indication that the remainder of the algorithm is working. To be thorough, two straight-and-level trajectories have been tested. The aircraft in the first trajectory flies away from the receiver, while the aircraft in the second trajectory flies broadside to the receiver. Notable differences in the results are observed.

The next scenario implements a constant-altitude, circular banked turn. Although this circular banked turn is not a realistic flight trajectory, it indicates that the algorithm is

able to perform when the aircraft power profiles become more complex. It also provides a more strenuous test of the coordinated flight model than the straight-and-level trajectories.

Finally, a flight profile recorded on-board a maneuvering F-15 at Edwards Air Force Base[1] is used to provide a more realistic test of the algorithm. The Edwards trajectory came complete with measured aircraft orientation, allowing a unique opportunity to quantify the performance degradation induced from having to estimate aircraft orientation. First, the algorithm is executed with the real aircraft orientation angles used in place of the ones estimated by the coordinated flight model. This serves as a baseline for comparison. Next, the simulation is run using the estimated aircraft orientation angles. Finally, a test is conducted in which the aircraft position is errantly estimated to be 300 m north and 300 m west of its actual location. This gauges performance degradation due to errors in the position estimates.

4.1 Straight-and-Level Trajectory # 1

The straight-and-level trajectory used in the first scenario contains targets moving at 200 m/s with altitudes of 8000 m. Recall that the targets in this maneuver are moving directly away from the receiver. As a relatively small number of aspects of the aircraft are visible to the receiver, it stands to reason that this represents a challenging scenario for the classification algorithm. The library profiles resulting from this maneuver are shown in Figure 12a. The four profiles are expected to look less similar when more aspects are presented to the receiver. The sharp dip in the profiles around 42 seconds is also worthy of comment. This might be troublesome if it were generated by FISC, but it is actually attributed to AREPS and the process used to model propagation.

The noise figure is swept from 30 dB to 100 dB, in increments of 5 dB, to gauge performance degradation as a function of noise power. One-hundred runs are executed using each aircraft as the detected target, for each noise figure. The percentage of incorrect identifications (probability of error) obtained for each aircraft model at each noise level is shown in

[1]The F-15C trajectory was obtained from the Joint Helmet Cuing System, Mission JH-16, conducted by the 445th Flight Test Squadron at Edwards Air Force Base in May 2000.

Figure 12b. This data is obtained from a set of Monte Carlo runs; thus the jumps in the curves are artificial and are expected to smooth out as the number of samples increase.

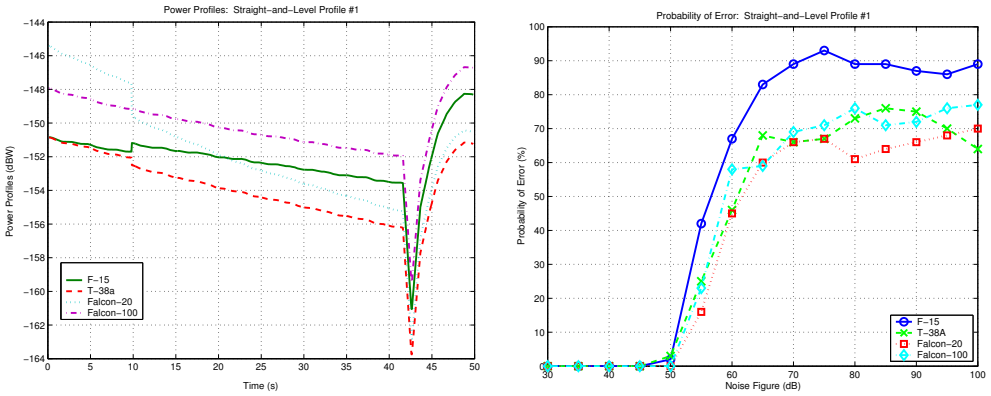

Figure 12: Straight-and-level flight profile #1: a.) power profiles (left), b.) probability of error vs. noise nigure (right).

Comparison of the probability of error plot with the plot of the power profiles provides insight into the viability of the algorithm. Figure 12a demonstrates that the algorithm performs perfectly until the noise figure reaches 50 dB. This corresponds to noise power of -151 dBW. Using the plot of the power profiles in Figure 12a, it is clear that this noise power is approximately equal to the maximum power of the signal. Once again, better performance might be expected if the power profiles looked less similar. This is likely to be the case when the aircraft flies broadside to the receiver, as more aspects will be presented to the receiver.

It is also noteworthy that the probability of error at high noise figures, for all four aircraft, is in the ballpark of 75%. This implies that when the signal is buried in the noise, the odds of the algorithm correctly identifying an aircraft are one in four; since there are four aircraft models in the target class, this is equivalent to chance.

Confusion matrices are tabulated to provide further insight into the types of mistakes being made by the algorithm. The aircraft listed in the first column correspond to the aircraft detected by the receiver. The aircraft listed across the top row pertain to the aircraft identified by the algorithm. The confusion matrices for this encounter, with noise figures of 50, 55, and 60 dB are shown in Tables 4 through 6.

Table 4: Confusion matrix for straight-and-level trajectory #1 with noise figure = 50 dB.

Aircraft	F-15	T-38A	Falcon-20	Falcon-100
F-15	98	1	0	1
T-38A	3	97	0	0
Falcon-20	0	0	100	0
Falcon-100	0	0	0	100

Table 5: Confusion matrix for straight-and-level trajectory #1 with noise figure = 55 dB.

Aircraft	F-15	T-38A	Falcon-20	Falcon-100
F-15	58	24	3	15
T-38A	21	75	3	1
Falcon-20	1	5	84	10
Falcon-100	14	3	6	77

Table 6: Confusion matrix for straight-and-level trajectory #1 with noise figure = 60 dB.

Aircraft	F-15	T-38A	Falcon-20	Falcon-100
F-15	33	34	13	20
T-38A	20	54	13	13
Falcon-20	10	19	55	16
Falcon-100	22	13	23	42

4.2 Straight-and-Level Trajectory # 2

The straight-and-level trajectory is then translated to a new location and rotated such that the aircraft flies broadside to the receiver. This seemingly minor change has a significant effect on the shape of the power profiles and, in turn, on algorithm performance. The power profiles and probability of error plots are shown in Figures 13a and 13b, respectively.

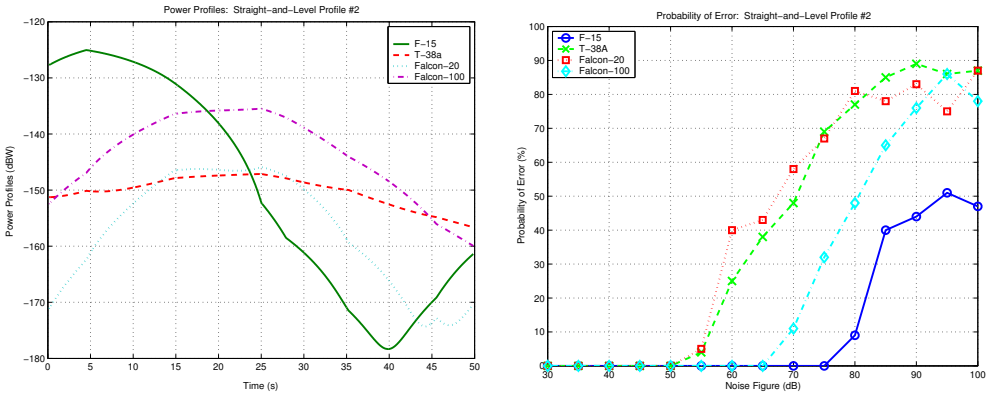

Figure 13: Straight-and-level flight profile #2: a.) power profiles (left), b.) probability of error vs. noise figure (right).

With this change in trajectory, the algorithm is able to correctly identify the aircraft at much higher noise levels. For example, the algorithm began misidentifying the F-15 in the first straight-and-level maneuver when the noise figure was 50 dB; here, in contrast, the algorithm does not begin incorrectly identifying the F-15 until the noise figure reaches 80 dB. The better performance is attributed to two factors. The primary cause is that the shape of the F-15 power profile is much more distinct from the other power profiles. A secondary factor is that the amplitude of the power profiles is larger, meaning that more noise is required to swamp the signal. These factors contribute to a lesser degree to the better performance with the Falcon-100. In the case of the other two aircraft, however, the power profiles look very similar to each other. This, coupled with the lack of increased signal amplitude, explains the lack of improved performance identifying the Falcon-20 and T-38A.

The confusion matrices for this maneuver, shown in Tables 7 through 9, reveal a dramatic pattern. Consider the first confusion matrix, for which the noise figure is 55 dB. Figure 13b

demonstrates that the only aircraft misidentified by the algorithm at this noise level are the T-38A and Falcon-20. The confusion matrix reveals that the misidentification errors are limited to swapping the T-38A and Falcon-20. Neither of these aircraft are mistakenly identified as the F-15 or Falcon-100. This pattern continues in Table 8. In this case, the only aircraft not being misidentified is the F-15. As before, the T-38A, Falcon-20, and Falcon-100, though misidentified by the algorithm, are never misidentified as the F-15. This pattern implies that the algorithm's main error is to swap aircraft whose power profiles have comparable amplitude. This swapping begins to occur when the maximum signal power generated by the aircraft becomes buried in the noise.

Table 7: Confusion matrix for straight-and-level trajectory #2 with noise figure = 55 dB.

Aircraft	F-15	T-38A	Falcon-20	Falcon-100
F-15	100	0	0	0
T-38A	0	96	4	0
Falcon-20	0	5	95	0
Falcon-100	0	0	0	100

Table 8: Confusion matrix for straight-and-level trajectory #2 with noise figure = 70 dB.

Aircraft	F-15	T-38A	Falcon-20	Falcon-100
F-15	100	0	0	0
T-38A	0	52	40	8
Falcon-20	0	50	42	8
Falcon-100	0	2	9	89

Table 9: Confusion matrix for straight-and-level trajectory #2 with noise figure = 80 dB.

Aircraft	F-15	T-38A	Falcon-20	Falcon-100
F-15	91	3	0	6
T-38A	16	23	19	42
Falcon-20	15	24	19	42
Falcon-100	17	17	14	52

4.3 Bank-Turn Trajectory

The constant-altitude circular banked turn provides a more difficult test of the algorithm. In this case, the target velocity is 100 m/s, and the altitude is 8000 m. Like the straight-and-level profiles, this is an idealized maneuver, rather than one recorded during an actual flight. Unlike the straight-and-level maneuver, this trajectory requires the coordinated flight model to estimate non-zero aircraft roll. The power profiles and probability of error curves are shown in Figures 14a and 14b.

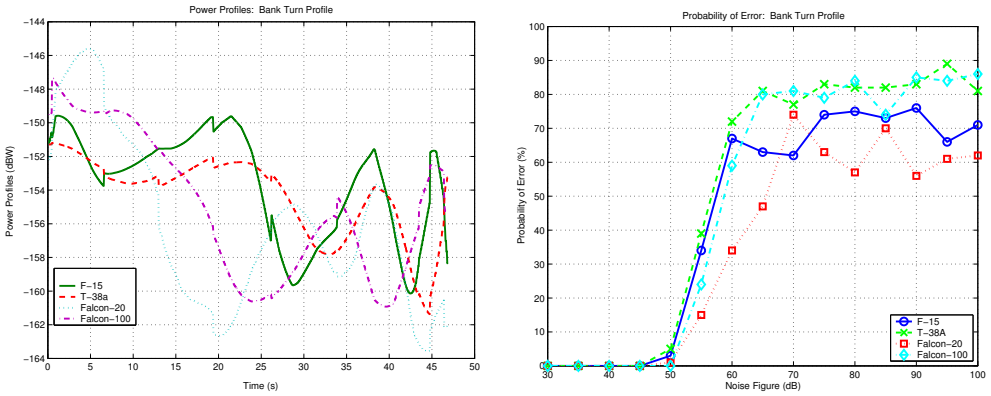

Figure 14: Constant-altitude circular banked turn: a.) power profiles (left), b.) probability of error vs. noise figure (right).

In this case, the maximum signal power is roughly -150 dBW for all four aircraft models. Thus, algorithm performance is expected to be excellent for all four aircraft until the noise figure rises above 50 dB. Figure 14b supports this claim. Also note that the probability of error curves are more tightly clustered around 75% at high noise levels than before. This is attributed to the fact that the power profiles generated by all four aircraft have comparable amplitudes. Using the pattern described in Section 4.2, the swapping errors made by the algorithm are expected to encompass all four aircraft models. The confusion matrices, shown in Tables 10 through 12, confirm this suspicion.

4.4 Edwards Trajectory

To gauge the performance of the algorithm when the target is maneuvering, the third test uses the Edwards trajectory. During the maneuver, the target changes altitudes and

Table 10: Confusion matrix for the banked turn trajectory with noise figure = 50 dB.

Aircraft	F-15	T-38A	Falcon-20	Falcon-100
F-15	97	3	0	0
T-38A	5	95	0	0
Falcon-20	0	0	99	1
Falcon-100	0	0	0	100

Table 11: Confusion matrix for the banked turn trajectory with noise figure = 60 dB.

Aircraft	F-15	T-38A	Falcon-20	Falcon-100
F-15	33	19	22	26
T-38A	19	28	27	26
Falcon-20	4	9	66	21
Falcon-100	7	13	39	41

Table 12: Confusion matrix for the banked turn trajectory with noise figure = 70 dB.

Aircraft	F-15	T-38A	Falcon-20	Falcon-100
F-15	38	22	23	17
T-38A	36	23	24	17
Falcon-20	32	22	26	20
Falcon-100	33	22	26	19

executes turns with varying degrees of curvature. This maneuver is shown in Figure 5 from both 3-D and 2-D perspectives, and was previously used to test the coordinated flight model.

To generate a baseline for comparison, this algorithm is first run using the known aircraft orientation angles. This essentially removes the coordinated flight model, and any error it induces, from the process. This test is then redone using the full algorithm, including the coordinated flight model. To simulate the possibility that the position estimates obtained from the passive radar system contain errors, a third test in conducted in which the estimated aircraft position is translated 300 m north and 300 m west. During this final test, the algorithm attempts to recognize targets while assuming these incorrect position estimates are correct.

The power profiles and probability of error curves generated for the F-15 under the three different tests are shown in Figures 15a and 15b, respectively. Although the power profiles show some marked deviations when the orientation angles are estimated and when the position errors are included, the probability of error curves corresponding to the three tests are remarkably similar. In fact, there seems to be little degradation in performance due to using the coordinated flight model, even in the presence of position errors. This is also true for the T-38 and Falcon-100, whose plots are shown in Figures 16 and 17, respectively.

The only aircraft for which degradation in performance is noted is the Falcon-20. Even in this case, the performance is nearly identical when the estimated orientation angles are substituted for the actual ones. The only performance degradation occurs when the errant positions are used to estimate the orientation angles. The power profiles and probability of error plots for the Falcon-20 appear in Figure 18.

The confusion matrices obtained with a noise figure of 60 dB are shown in Tables 13 through 15. To get a better sense of the differences in algorithm performance between the three tests, we computed the percentage of total errors. For a noise figure of 60 dB, the algorithm is correct 97% of the time when the orientation angles are known, 92% of the time when the orientation angles are estimated from correct positions, and 90% of the time when incorrect position estimates are used.

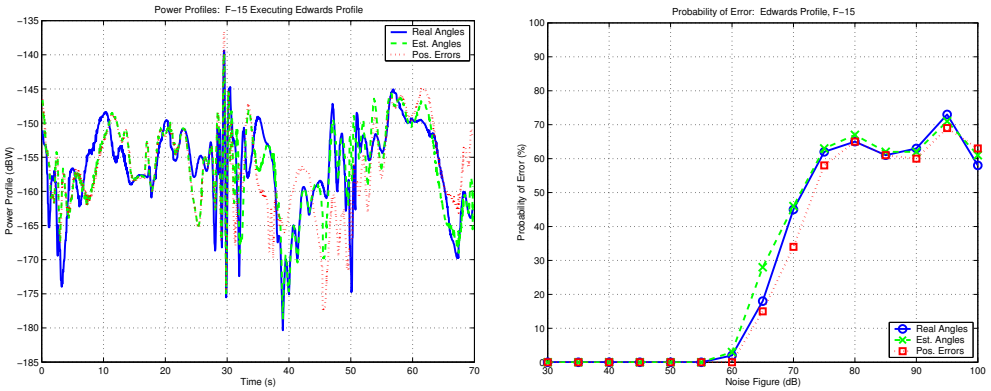

Figure 15: F-15 executing the Edwards trajectory: a) power profiles (left), b) probability of error (right).

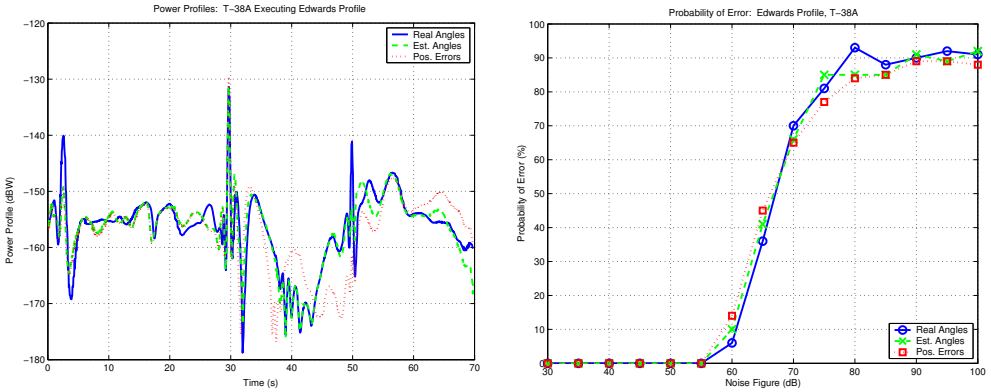

Figure 16: T-38A executing the Edwards trajectory: a) power profiles (left), b) probability of error (right).

Although performance degrades significantly when the noise figure increases to 70 dB, the results of the three tests remain similar to each other. At a noise figure of 70 dB, the algorithm is correct 46% of the time when the correct orientation angles are used, 49% of the time when the estimated orientation angles are used, and 46% of the time when incorrect positions are used to estimate the orientation angles. Confusion matrices corresponding to these three tests are displayed in Tables 16 through 18.

Table 13: Confusion matrix for the Edwards trajectory with noise figure = 60 dB, using real orientation angles.

Aircraft	F-15	T-38A	Falcon-20	Falcon-100
F-15	98	0	0	2
T-38A	1	94	0	5
Falcon-20	0	0	100	0
Falcon-100	0	6	0	94

Table 14: Confusion matrix for the Edwards trajectory with noise figure = 60 dB, using estimated orientation angles.

Aircraft	F-15	T-38A	Falcon-20	Falcon-100
F-15	97	1	0	2
T-38A	2	90	0	8
Falcon-20	0	0	100	0
Falcon-100	1	17	0	82

Table 15: Confusion matrix for the Edwards trajectory with noise figure = 60 dB, using incorrect position estimates.

Aircraft	F-15	T-38A	Falcon-20	Falcon-100
F-15	100	0	0	0
T-38A	3	86	0	11
Falcon-20	0	1	96	3
Falcon-100	3	18	0	79

Table 16: Confusion matrix for the Edwards trajectory with noise figure = 70 dB, using real orientation angles.

Aircraft	F-15	T-38A	Falcon-20	Falcon-100
F-15	55	20	10	15
T-38A	31	30	21	18
Falcon-20	7	11	75	7
Falcon-100	32	25	21	22

Table 17: Confusion matrix for the Edwards trajectory with noise figure = 70 dB, using estimated orientation angles.

Aircraft	F-15	T-38A	Falcon-20	Falcon-100
F-15	54	16	16	14
T-38A	27	34	22	17
Falcon-20	10	7	80	3
Falcon-100	30	24	21	25

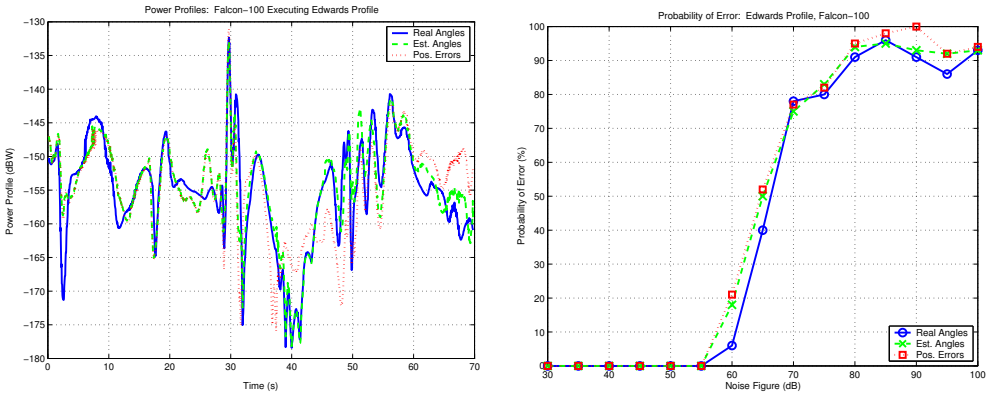

Figure 17: Falcon-100 executing the Edwards trajectory: a) power profiles (left), b) probability of error (right).

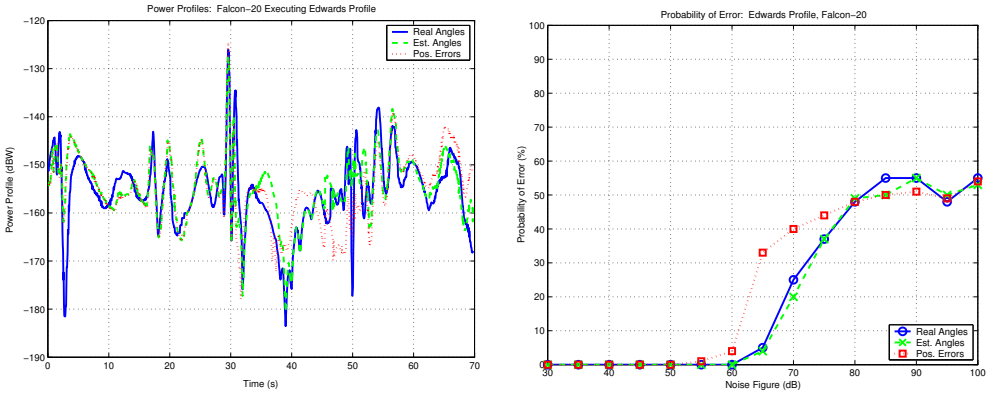

Figure 18: Falcon-20 executing the Edwards trajectory: a) power profiles (left), b) probability of error (right).

Table 18: Confusion matrix for the Edwards trajectory with noise figure = 70 dB, using incorrect position estimates.

Aircraft	F-15	T-38A	Falcon-20	Falcon-100
F-15	66	17	6	11
T-38A	36	35	13	16
Falcon-20	15	17	60	8
Falcon-100	37	27	13	23

CHAPTER V

RESULTS OBTAINED USING HH POLARIZATION

As in the previous chapter, three scenarios of increasing complexity are used to test the algorithm. The simplest of the three scenarios involves an aircraft flying in a straight-and-level path directly away from the receiver. A variation of this maneuver is also conducted in which the aircraft heading is rotated by 90^o such that it flies broadside to the receiver. The aircraft in the second scenario executes a constant-altitude, constant-velocity, circular banked turn. Although this second maneuver is not terribly realistic, it provides a more strenuous test of the algorithm than the first maneuver, and builds the complexity of testing towards the final maneuver. The final maneuver used to test the algorithm is a flight profile recorded on-board a maneuvering F-15 at Edwards Air Force Base[1]. This Edwards trajectory was provided complete with measured aircraft orientation, allowing us a unique opportunity to quantify performance degradation attributed to the estimation of aircraft orientation. First, the measured orientation angles are used to establish a baseline for algorithm performance. Then, the simulation is redone using the estimated orientation angles in place of the real ones. Finally, to gauge performance degradation caused by errors in the position estimates, the test is redone using aircraft positions that are errantly estimated to be 300 m north and 300 m west of the actual locations. All of the maneuver trajectories are shown in Figure 11.

5.1 Straight-and-Level Trajectory # 1

The power profiles generated for all four aircraft in the target class are shown in Figure 19a. Since this simulation uses the same propagation loss profile as Section 4.1, it contains the same artifact at 42 seconds. The probability of error curve for this maneuver is shown

[1]The F-15C trajectory was obtained from the Joint Helmet Cuing System, Mission JH-16, conducted by the 445th Flight Test Squadron at Edwards Air Force Base in May 2000.

in Figure 19b.

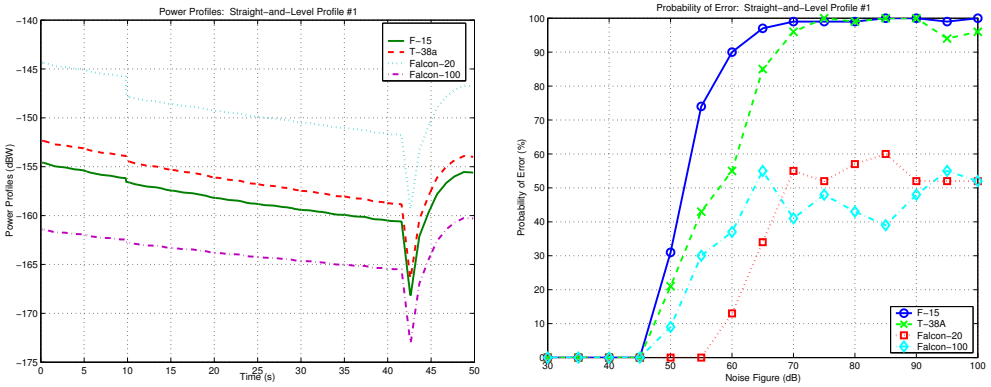

Figure 19: Straight-and-level flight profile #1: a.) power profiles (left), b.) probability of error vs. noise figure (right).

As is clear from Figure 19b, the algorithm performs perfectly when the noise figure is less than 50 dB. Errors in target identification are first noted for the F-15, T-38A, and Falcon-100 when the noise figure is 50 dB, and a rapid decline in performance is noted as the noise figure increases beyond 50 dB. Despite identification errors of the other three aircraft, the algorithm is able to perfectly identify the Falcon-20 for noise figures up to N_F = 55 dB. A quick glance at Figure 19a reveals the cause of the better performance. While the F-15, T-38A, and Falcon-100 have maximum signal power of approximately -155 dBW, the maximum signal power of the Falcon-20 is approximately -145 dBW. This differentiates its profile from the others. As is the case when the antennas are vertically polarized, the more variations exist between the power profiles, the better the algorithm is able to identify the aircraft. Confusion matrices for this encounter, with noise figures of 50, 55, and 60 dB are shown in Tables 19 through 21.

In addition to being the most likely aircraft to be correctly identified when present at these noise levels, the Falcon-20 is the least likely to be mistakenly identified as the target.

5.2 Straight-and-Level Trajectory # 2

The test is then repeated with the second straight-and-level trajectory. The effects of changing aircraft position and heading are largely dependent upon aircraft type. The maximum

Table 19: Confusion matrix for straight-and-Level trajectory #1 with noise figure = 50 dB.

Aircraft	F-15	T-38A	Falcon-20	Falcon-100
F-15	69	17	0	14
T-38A	21	79	0	0
Falcon-20	0	0	100	0
Falcon-100	9	0	0	91

Table 20: Confusion matrix for straight-and-level trajectory #1 with noise figure = 55 dB.

Aircraft	F-15	T-38A	Falcon-20	Falcon-100
F-15	26	36	0	38
T-38A	30	57	1	12
Falcon-20	0	0	100	0
Falcon-100	22	8	0	70

Table 21: Confusion matrix for straight-and-level trajectory #1 with noise figure = 60 dB.

Aircraft	F-15	T-38A	Falcon-20	Falcon-100
F-15	10	36	5	49
T-38A	7	45	6	42
Falcon-20	0	13	87	0
Falcon-100	14	23	0	63

signal power of the F-15 rises from -155 dBW in the first encounter to approximately -145 dBW. The maximum signal power of the remaining three aircraft falls between -140 and -135 dBW.

Because this path shows a greater diversity of aspect angles on the target, we might expect performance in this encounter to improve for all of the aircraft models. A comparison of Figures 19b and 20b supports this claim. In this test, the algorithm performs perfectly for noise figures up to N_F= 60 dB. Once again, this is approximately the point at which the maximum noise power overtakes the maximum signal power.

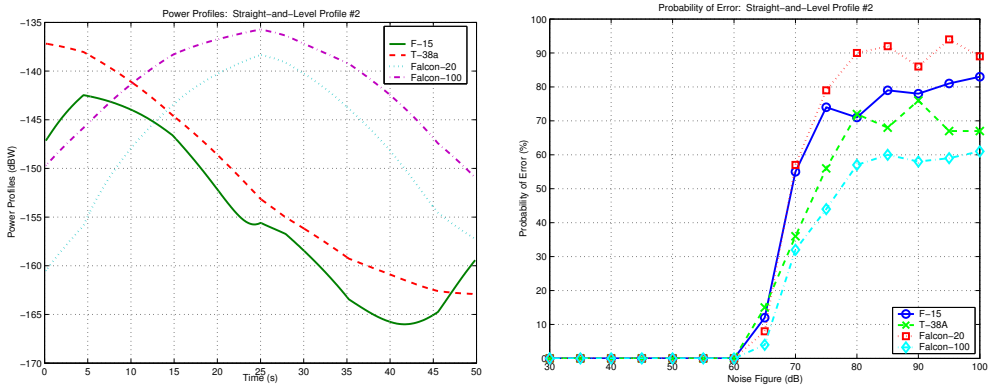

Figure 20: Straight-and-level flight profile #2: a.) power profiles (left), b.) probability of error vs. noise figure (right).

The confusion matrices corresponding to noise figures of 65, 70, and 75 dB are shown in Tables 22 through 24. A familiar pattern emerges in these confusion matrices. For a noise figure of 55 dB, the algorithm does not just exhibit non-zero probability of error for the Falcon-20 and T-38A; when it misidentifies these two aircraft, it swaps them. This trend continues until the noise figure reaches 70 dB, the point at which the algorithm begins incorrectly identifying the Falcon-100. At that point, a small number of the T-38A and Falcon-20 cases begin to be misidentified as the Falcon-100. None of the aircraft are misidentified as the F-15 until the noise figure reaches 80 dB. Again, this corresponds to the point at which the algorithm begins to mistake the F-15 for other aircraft. In this case, the likelihood of an aircraft model being incorrectly classified as another model and the likelihood of being falsely identified occur at the same noise levels.

Table 22: Confusion matrix for straight-and-level trajectory #2 with noise figure = 65 dB.

Aircraft	F-15	T-38A	Falcon-20	Falcon-100
F-15	88	9	3	0
T-38A	15	85	0	0
Falcon-20	4	1	92	3
Falcon-100	0	0	4	96

Table 23: Confusion matrix for straight-and-level trajectory #2 with noise figure = 70 dB.

Aircraft	F-15	T-38A	Falcon-20	Falcon-100
F-15	45	27	24	4
T-38A	16	64	14	6
Falcon-20	20	18	43	19
Falcon-100	2	7	23	68

Table 24: Confusion matrix for straight-and-level trajectory #2 with noise figure = 75 dB.

Aircraft	F-15	T-38A	Falcon-20	Falcon-100
F-15	26	34	17	23
T-38A	19	44	14	23
Falcon-20	17	26	21	36
Falcon-100	8	21	15	56

5.3 Bank-Turn Trajectory

The library profiles resulting from the bank turn maneuver are shown in Figure 21a. The probability of error is shown as a function of noise figure in Figure 21b. This time, the maximum signal power from each of the four aircraft is approximately -145 dBW. This suggests that the performance will be similar for all four aircraft models. It seems unlikely that any of the aircraft will be favored over others. The confusion matrices, shown in Tables 25 through 27, validate this prediction; the errors are more evenly distributed over the various aircraft models than in the second straight-and-level encounter.

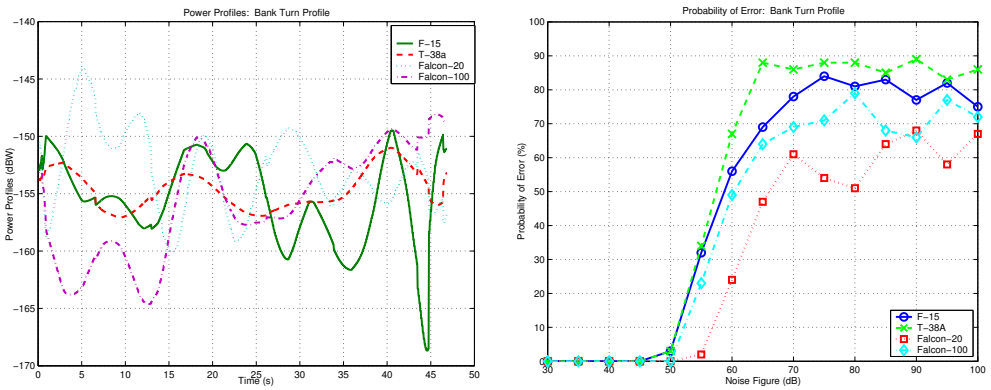

Figure 21: Constant-altitude circular banked turn: a.) power profiles (left), b.) probability of error vs. noise figure (right).

5.4 Edwards Trajectory

Finally, the three tests conducted with the Edwards trajectory are redone with horizontally polarized transmit and receive antennas. Recall that the first test is a baseline in which the correct aircraft orientation angles are used to compute the library power profiles. The second test uses the coordinated flight model to estimate aircraft orientation, given the correct aircraft position profiles. The third test uses incorrect position estimates as well as the estimated orientations. The power profiles generated under all three tests for the F-15 are shown in Figure 22a. The corresponding probability of error curves are presented in Figure 22b. Performance is very similar under all three tests.

Similar plots are shown in Figures 23a and 23b, now using the T-38A as the true target.

Table 25: Confusion matrix for the banked turn trajectory with noise figure = 50 dB.

Aircraft	F-15	T-38A	Falcon-20	Falcon-100
F-15	97	3	0	0
T-38A	3	97	0	0
Falcon-20	0	0	100	0
Falcon-100	0	0	0	100

Table 26: Confusion matrix for the banked turn trajectory with noise figure = 60 dB.

Aircraft	F-15	T-38A	Falcon-20	Falcon-100
F-15	44	19	14	23
T-38A	25	33	15	27
Falcon-20	8	10	76	6
Falcon-100	20	17	12	51

Table 27: Confusion matrix for the banked turn trajectory with noise figure = 70 dB.

Aircraft	F-15	T-38A	Falcon-20	Falcon-100
F-15	22	14	36	28
T-38A	22	14	36	28
Falcon-20	22	11	39	28
Falcon-100	20	13	36	31

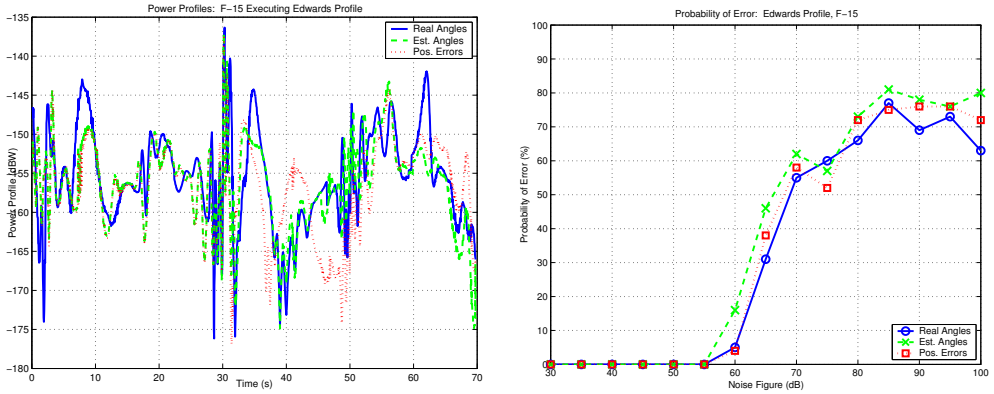

Figure 22: F-15 executing the Edwards trajectory: a) power profiles (left), b) probability of error (right).

Once again, the algorithm performance is strikingly similar under all three conditions. This trend holds for the Falcon-100, whose curves are presented in Figure 24. The only time that any large difference in performance is noted amongst the three tests occurs when the Falcon-20 is used. In that case, the Falcon-20 is incorrectly identified as the Falcon-100 when the estimated orientation angles are used. The curves for the Falcon-20 are shown in Figure 25.

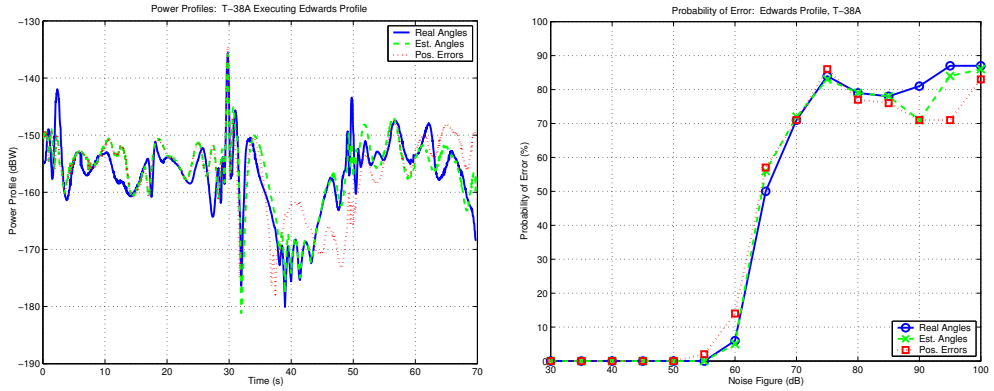

Figure 23: T-38A executing the Edwards trajectory: a) power profiles (left), b) probability of error (right).

Confusion matrices for a noise figure of 60 dB are shown in Tables 28 through 30. Averaged over all four aircraft types, the algorithm has an accuracy rate of 97% at this noise level when the aircraft orientation angles are known, 64% when the coordinated flight

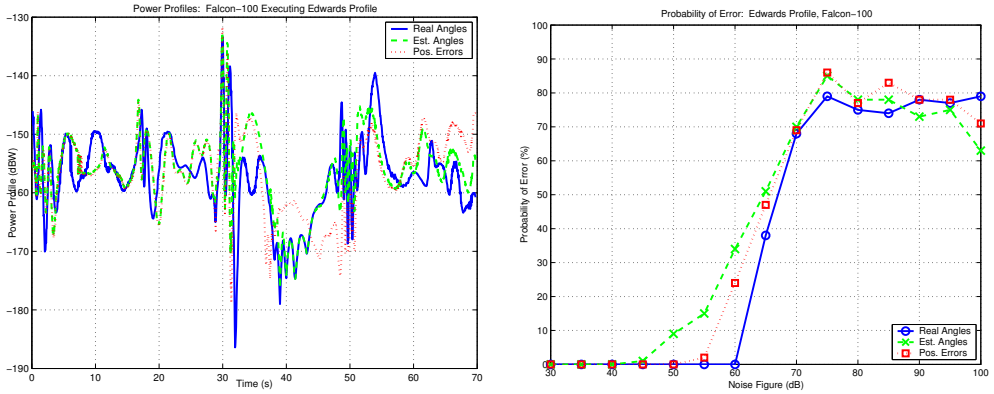

Figure 24: Falcon-100 executing the Edwards trajectory: a) power profiles (left), b) probability of error (right).

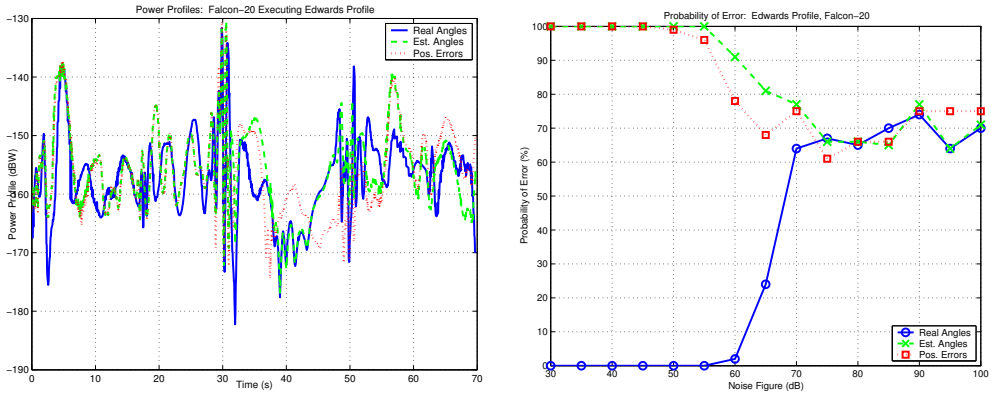

Figure 25: Falcon-20 executing the Edwards trajectory: a) power profiles (left), b) probability of error (right).

model is used to estimate aircraft orientation, and 70% when the incorrect position estimates are used. The gap in performance between the first and the second two cases is largely due to the algorithm's difficulty with the Falcon-20. When the Falcon-20 is removed from the analysis, the accuracy rate of the algorithm is 96% using the correct orientation angles, 82% using the estimated orientation angles, and 86% using the incorrect position estimates. Note that using incorrect positions, in addition to incorrect orientations, seems to do better than using incorrect orientations with correct positions in these particular cases. This difference is probably not statistically significant.

As the noise figure increases to 70 dB, the results of all three tests become increasingly similar. Averaging over all four aircraft models, the algorithm has an accuracy rate of 36%

when using the real orientation angles, 30% when using the estimated orientation angles, and 32% when the position estimates are incorrect. The confusion matrices corresponding to these three tests are shown in Tables 31 through 33.

Figure 25b vividly illustrates the difficulties which may arise from not estimating the orientation angles with enough accuracy; when using the estimated orientation angles at low noise levels, the Falcon-20 is *never* correctly identified. The Falcon-20 at the estimated orientation looks more like the Falcon-100 at the correct orientation than the Falcon-20 at the correct orientation! The model is so far off that increasing levels of noise actually yield better performance. In fact, the best performance, occurring at the *highest* noise levels, is that which would be achieved by randomly picking one of the four targets without looking at the data. To avoid such catastrophic model mismatches, we are currently exploring methods to jointly estimate the orientation and target type from the data.

Table 28: Confusion matrix for the Edwards trajectory with noise figure = 60 dB, using real orientation angles.

Aircraft	F-15	T-38A	Falcon-20	Falcon-100
F-15	95	3	1	1
T-38A	3	94	1	2
Falcon-20	0	1	98	1
Falcon-100	0	0	0	100

Table 29: Confusion matrix for the Edwards trajectory with noise figure = 60 dB, using estimated orientation angles.

Aircraft	F-15	T-38A	Falcon-20	Falcon-100
F-15	84	15	0	1
T-38A	4	95	0	1
Falcon-20	0	15	9	76
Falcon-100	10	24	0	66

Table 30: Confusion matrix for the Edwards trajectory with noise figure = 60 dB, using incorrect position estimates.

Aircraft	F-15	T-38A	Falcon-20	Falcon-100
F-15	96	4	0	0
T-38A	11	86	0	3
Falcon-20	0	10	22	68
Falcon-100	12	12	0	76

Table 31: Confusion matrix for the Edwards trajectory with noise figure = 70 dB, using real orientation angles.

Aircraft	F-15	T-38A	Falcon-20	Falcon-100
F-15	45	20	17	18
T-38A	36	29	21	14
Falcon-20	27	19	36	18
Falcon-100	30	20	18	32

Table 32: Confusion matrix for the Edwards trajectory with noise figure = 70 dB, using estimated orientation angles.

Aircraft	F-15	T-38A	Falcon-20	Falcon-100
F-15	38	18	21	23
T-38A	31	28	20	21
Falcon-20	23	15	23	39
Falcon-100	28	21	21	30

Table 33: Confusion matrix for the Edwards trajectory with noise figure = 70 dB, using incorrect position estimates.

Aircraft	F-15	T-38A	Falcon-20	Falcon-100
F-15	42	20	18	20
T-38A	30	29	21	20
Falcon-20	27	16	25	32
Falcon-100	30	16	23	31

CHAPTER VI

CONCLUSION

Passive radar is an emerging technology that is only beginning to be exploited by the scientific community. The addition of ATR capabilities can only enhance the effectiveness of these systems. While this task was attempted by Herman with a particle filtering scheme, the major contribution of this paper is that it demonstrates that good results are often possible with a simpler approach.

The results presented in this paper provide a good deal of insight into the viability of this algorithm. Whether the maneuver is simple or complex, very good performance is expected for targets at the simulated locations and anticipated noise levels. In fact, with the exception of the Falcon-20 case presented in Section 5.4, the identification results presented in this paper are perfect at the anticipated noise figure. Of course, we would not expect a real system to perform exactly as well as our simulations, since there will always be additional effects that cannot be easily modeled.

The results obtained when both antennas are vertically polarized indicate that as long as the targets fall within the receiver's main lobe and are sufficiently close in range, the algorithm will have little trouble identifying them. Performance can then be expected to decline for aircraft whose trajectories do not cross through the receiver's main lobe, or whose position is too far away from the system to generate sufficient SNR. The range required to generate sufficient SNR is itself dependent upon the target type and orientation.

The results obtained using horizontally polarized antennas are slightly less encouraging, and indicate that the coordinated flight model should be tweaked as part of future work, to ensure excellent performance under a wide variety of conditions. An additional topic for future work is the expansion of the FISC database via sparse sampling techniques.

REFERENCES

[1] Barton, D., *Modern Radar System Analysis.* Artech House, 1988.

[2] Chen, J. and Walton, E., "Comparison of two target classification techniques," *IEEE Trans. on Aerospace and Electronic Systems*, vol. 22, pp. 15–21, Jan. 1986.

[3] Doucet, A., de Freitas, N., and Gordon, N., *Sequential Monte Carlo Methods in Practice.* Springer-Verlag, 2001.

[4] Ehrman, L. and Lanterman, A., "Automated target recogntion using passive radar and coordinated flight models," in *Automatic Target Recognition XIII*, vol. SPIE Proc. 5094, (Orlando, FL), April 2003.

[5] Ehrman, L. and Lanterman, A., "Estimation of aircraft orientation from flight paths using a coordinated flight model," *submitted to IEEE Transactions on Aerospace and Electronic Systems*, November 2002.

[6] Griffiths, H. and Long, N., "Television-based bistatic radar," *IEE Proceedings, Part F*, vol. 133, pp. 649–657, December 1986.

[7] Herman, S. and Moulin, P., "A particle filtering approach to joint radar tracking and automatic target recognition," in *Proc. IEEE Aerospace Conference*, (Big Sky, Montana), March 10-15 2002.

[8] Herman, S., *A Particle Filtering Approach to Joint Passive Radar Tracking and Target Classification.* Urbana, IL: Doctoral Dissertation, Department of Electrical and Computer Engineering, Univ. of Illinois at Urbana-Champaign, 2002.

[9] Howland, P., "Target tracking using television-based bistatic radar," *IEE Proc. F: Radar, Sonar, and Navigation*, vol. 146, pp. 166–174, June 1999.

[10] Jacobs, S. and O'Sullivan, J., "Automatic target recognition using sequences of high resolution radar range-profiles," *IEEE Trans. on Aerospace and Electronic Systems*, vol. 36, no. 2, pp. 364–382, 2000.

[11] Kuethe, A. and Chow, C.-Y., *Foundations of Aerodynamcis: Bases of Aerodynamic Design, 3rd Edition.* John Wiley & Sons, 1976.

[12] Lanterman, A., "Tracking and recognition of airborne tagets via commercial television and fm radio signals," in *Acquisition, Tracking, and Pointing XIII* (Masten, M. and Stockum, L., eds.), vol. SPIE Proc. 3692, (Orlando, FL), pp. 189–198, April 1999.

[13] Lin, H. and Ksienski, A., "Optimum frequencies for aircraft classification," *IEEE Trans. on Aerospace and Electronic Systems*, vol. 17, pp. 656–665, Sept. 1981.

[14] Lin, Y. and Ksienski, A., "Identification of complex geomtrical shapes by means of low-frequency radar returns," *The Radio and Electronic Engineer*, vol. 46, pp. 472–486, Oct. 1976.

[15] M. A. Ringer, G. J. F. and Anderson, S. J., "Waveform analysis of transmitters of opportunity for passive radar," *Surveillance Systems Division, Electronics and Surveillance Research Laboratory.*

[16] Mensa, D., "Radar imaging," *International Journal of Imaging Systems and Technology*, vol. 4, pp. 148–163, 1992.

[17] Meyer, C. and Gibson, D., *Route Surveying and Design, 5th Edition.* Harper & Row, Publishers, 1980.

[18] Sahr, J. and Lind, F., "The Manastash ridge radar: A passive bistatic radar for upper atmospheric radio science," *Radio Science*, pp. 2345–2358, Nov.-Dec. 1997.

[19] Sahr, J. and Lind, F., "Passive radio remote sensing of the atmosphere using transmitters of opportunity," *Radio Science*, pp. 4–7, March 1998.